

PAPER • OPEN ACCESS

Individualized defocusing particle tracking for dynamic surface profilometry

To cite this article: Sean MacKenzie *et al* 2025 *Meas. Sci. Technol.* **36** 056005

View the [article online](#) for updates and enhancements.

You may also like

- [Intrafractional 3D localization using kilovoltage digital tomosynthesis for sliding-window intensity modulated radiation therapy](#)
Pengpeng Zhang, Margie Hunt, Hai Pham et al.
- [3D–2D registration for surgical guidance: effect of projection view angles on registration accuracy](#)
A Uneri, Y Otake, A S Wang et al.
- [A novel feature points extraction method for defocused camera calibration based on phase-shift circular fringes](#)
Yi Zhang, Jiuwei Yu, Jing Sun et al.

Individualized defocusing particle tracking for dynamic surface profilometry

Sean MacKenzie^{*} , Alexander Eden , David E Huber  and Sumita Pennathur 

Department of Mechanical Engineering, University of California Santa Barbara, Santa Barbara, CA 93106, United States of America

E-mail: sean_mackenzie@ucsb.edu

Received 13 November 2024, revised 7 April 2025

Accepted for publication 15 April 2025

Published 7 May 2025



Abstract

Three-dimensional (3D) localization and single-particle tracking (SPT) are powerful techniques for characterizing shape, motion, and deformation of materials. However, these methods often require complex optical setups that demand expert use, limiting their accessibility to the wider scientific community. This paper presents a new technique called individualized defocusing particle tracking (IDPT), which uses intrinsic aberrations in ordinary lab microscopes to perform 3D surface measurements at camera frame rates. The IDPT technique comprises a simple *in-situ* calibration procedure and 3D localization algorithm that leverages particles' unique defocusing patterns to enhance measurement sensitivity while compensating for optics-induced bias errors. Our empirical approach implicitly transforms systematic optical effects—including those caused by misalignment or defects of optical elements—into valuable sources of positional information, allowing our method to work with common lab microscopes. We validate the IDPT technique through synthetic and benchtop experiments involving rigid body motion of a planar substrate and the dynamic deformation of elastic discs, demonstrating that our algorithm surpasses comparable SPT algorithms in accuracy and resolution. The IDPT technique is simple yet robust, offering broad applicability for dynamic surface profilometry and deformation analysis.

Keywords: defocusing particle tracking, optical microprofilometry, 3D localization microscopy, strain field measurement

1. Introduction

Optical techniques for measuring surface topography, deformation, and strain are essential tools across various scientific fields, including semiconductor manufacturing, biological imaging, and materials science [1–4]. Techniques such as stereo digital image correlation (DIC), tomographic imaging, confocal microscopy, and interferometry enable precise three-dimensional (3D) characterization of surfaces. However,

these techniques are constrained by practical challenges when applied to micro- and nanoscale phenomena, such as limited optical access, complex imaging environments, and the need for rapid data acquisition to capture dynamic systems [5]. For example, stereo DIC relies on multiple camera perspectives to measure surface deformations, but it requires precise camera alignment and is sensitive to lighting conditions. Tomographic imaging reconstructs 3D images from two-dimensional (2D) slices, offering detailed insights into internal features but at the cost of being computationally intensive and time-consuming. Confocal microscopy and interferometry provide excellent resolution but rely on scanning procedures that limit temporal

* Author to whom any correspondence should be addressed.



resolution. Furthermore, these techniques typically require specialized equipment and complicated calibration and validation procedures, which limit their accessibility for broader use.

3D localization and single-particle tracking (SPT) encompass a class of powerful and versatile optical microscopy techniques that can address these limitations [6–10]. Principally, SPT describes the localization of single micro- or nanoscopic objects (e.g. particles) in three spatial dimensions from 2D images. Localization of particles on a surface allows reconstruction of topography and repeated localizations over time allows tracking of motion and local deformation [11–15]. Compared to conventional 3D optical techniques, the key advantages of SPT are high-speed, scan-free acquisition at camera frame rates, applicability to a wide range of sample types and depth ranges, and the fact that many SPT techniques can be implemented as add-ons to standard light microscopes. Defocusing particle tracking (DPT) is one technique that utilizes the degree of defocusing in images of particles to infer their distance from the focal plane [16, 17]. DPT offers several practical advantages: it fundamentally requires only basic optical components—typically a microscope and a camera—and can be adapted to various measurement objects (e.g. cells [18, 19]) and illumination modalities, provided there is sufficient image contrast and reliable defocusing patterns.

To determine 3D position from 2D images, DPT typically relies on a calibration model that provides a mapping of defocusing characteristics, such as size, shape, and pattern, to corresponding depth positions. Most often, generalized calibration models are used, which uniformly apply a single mapping to the entire imaging field. However, this approach can introduce biases due to variations in individual particle appearances and non-uniform optical effects [20, 21]. These errors can be mitigated to some extent by quantifying and correcting biases during post-processing [22, 23], but this approach is less than ideal, as it requires both comparison against an objective truth and fitting interpolant models in two or three dimensions, which is subject to the quality of the underlying data [24–28]. A more sophisticated approach involves local calibrations that incorporate spatially-varying optical effects into the calibration model, thus compensating for systematic errors during pre-processing [29–32]. Although local calibration models have been shown to improve accuracy, they have been considered computationally complex and challenging to implement [33], resulting in limited adoption.

Despite the fundamental simplicity of DPT, most current methods require modifications to conventional optical systems to more efficiently encode depth information into defocused images. This need arises because, in an unaberrated optical system, defocusing patterns are symmetric above and below the focal plane, leading to ambiguity in determining the direction of displacement along the optical axis. To address this, custom optics are used to introduce extrinsic asymmetry. While this approach can improve performance [34, 35], it adds cost and complexity, and can exacerbate bias errors if not properly accounted for [36]. These factors can deter researchers who may lack the expertise or would prefer not to modify their equipment.

Although several promising examples of DPT using common lab microscopes have been documented [37–39], achieving reliable measurement results using standard optical systems remains a key challenge in the field. More broadly, there remains demand for 3D surface measurement methods that are accessible, user-friendly, and widely applicable. Thus, we believe the community would benefit from a simple yet robust technique that offers consistent measurement performance without the burden of bespoke optical configurations or computationally demanding analysis and bias-correction routines.

To address this unmet need, we developed individualized DPT (IDPT), a 3D particle tracking technique and algorithm for surface measurements using ordinary lab microscopes. The IDPT technique comprises a simple experimental procedure to capture *in-situ* calibration and evaluation images, and a localization algorithm that leverages each particle's unique defocusing patterns to accurately determine its position. Distinct from conventional DPT approaches based on global or local calibrations, IDPT combines calibration and 3D localization into an individual-particle tracking approach. Through IDPT's empirical-based method, we repurpose optical distortions and system aberrations, converting them into a valuable source of spatial information that makes our approach applicable to common microscopes. Although conceptually simple, the IDPT technique is highly effective, as it utilizes the complete information contained within particle images.

To validate IDPT, we separately imaged microparticles on a rigid planar substrate and on deformable elastic discs using a standard epifluorescence microscope and determined the particles' 3D positions using IDPT. We highlight the advantages of the IDPT algorithm by comparison against a custom-built DPT algorithm that follows the conventional, generalized approach—using a generalized calibration model. Our findings show that IDPT outperforms conventional DPT in key performance metrics, including measurement resolution and depth measurement sensitivity and accuracy. Our method is unique as it enables 3D surface measurements using an ordinary microscope and straightforward experimental setup, thus differentiating IDPT from traditional optical metrology techniques and more generalized 3D particle tracking methods requiring custom optical setups. In this work, we describe and validate the IDPT technique and make available a fully realized DPT software package (see [appendix](#)) with broad applications beyond those demonstrated herein.

2. The IDPT technique

Our measurement concept determines a particle's unknown position by comparing its image to reference images of the same particle taken at known positions. The accuracy of this approach depends on how closely features in the evaluation image (such as size, shape, and intensity) match those in the reference images [23, 33]. Our key insight is to maximize this objective through a combined approach to image acquisition and analysis: First, recording wide-field reference images *in-situ* preserves both the physical characteristics of

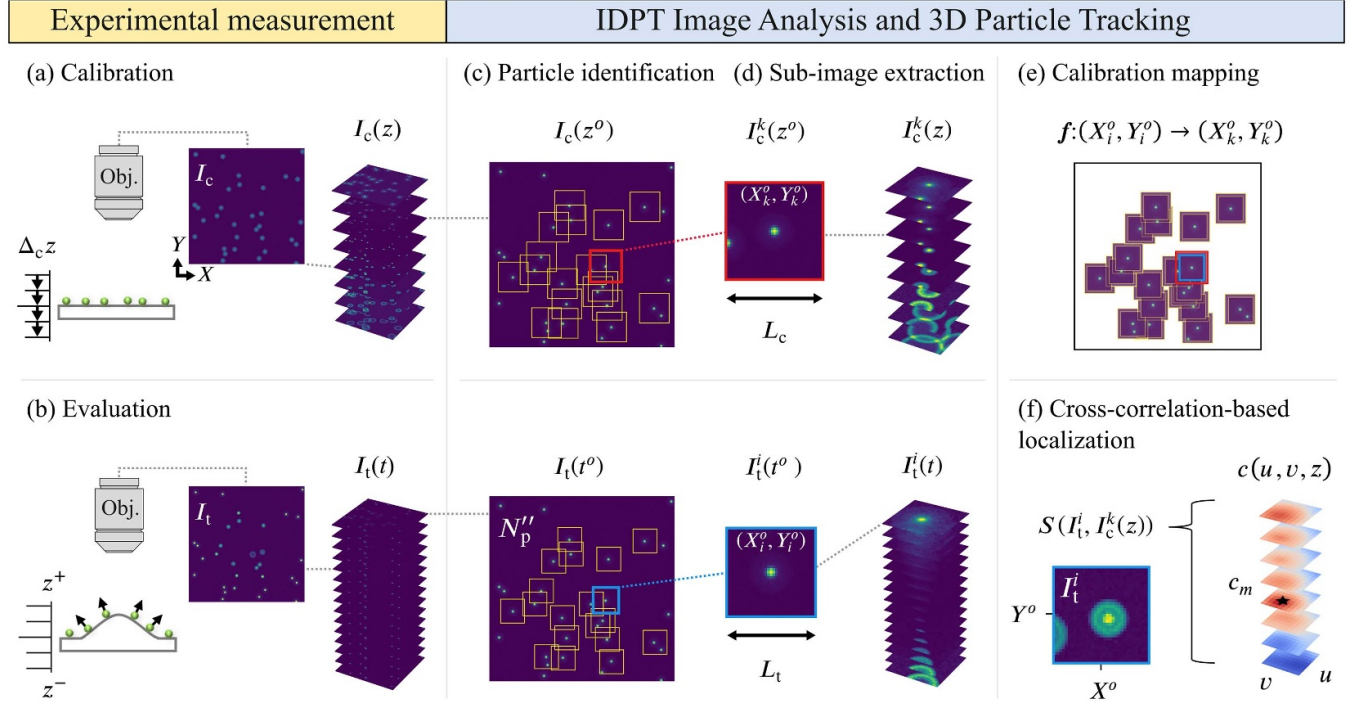


Figure 1. (a) A set of reference images capture particle defocusing patterns at discrete increments $\Delta_c z$ along the optical axis. (b) A set of evaluation images capture defocusing patterns over time t that encode local surface topography. (c) One calibration image and one test image are used to identify particles and determine their baseline positions (X^0, Y^0) . (d) The particles' sub-images are extracted from each frame to form calibration stacks $I_c^k(z)$ that map defocusing patterns to known 3D positions, and target particle stacks $I_t^i(t)$ that encode yet-to-be-determined 3D positions. (e) A mapping algorithm f assigns target particle stacks to calibration stacks using the particles' baseline positions. (f) A similarity function compares a target particle sub-image I_t^i against each sub-image in the assigned calibration stack, $S(I_t^i, I_c^k(z))$. The resulting stack of 2D similarity maps $c(u, v, z)$ is interpolated around the position of maximum similarity c_m (black star) to determine the particle's 3D position with sub-resolution accuracy. The particle shown in sub-image I_t^i is shifted off center (i.e. relative to (X^0, Y^0)) due to in-plane motion of the surface under test (shown in (b)), which is decoded by a corresponding off-center shift in the position of c_m . Synthetic particle images were generated using MicroSIG [40], using the settings given in note S3.

the measurement surface (e.g. particle size, shape, and position) and the optical system's effects (e.g. point spread function, distortion, and illumination variations). Second, these wide-field images can be analyzed on a per-particle basis by comparing each evaluation particle image to its corresponding set of reference particle images.

We realize this measurement concept through our IDPT technique, which uses this synergy to measure local surface displacements in deformable microsystems (e.g. soft microsystems). Image analysis is performed by our IDPT algorithm, incorporating design decisions guided by the assumptions outlined in table S1. These assumptions allow us to enhance the measurement performance of IDPT for this specific use case while simplifying the software implementation. Our algorithm is based on the recognition that, although particle images across the field of view may show significant variations (due to particle-to-particle differences in size or shape, spatially varying optical effects, or overlapping defocusing patterns), any single particle image is primarily influenced by the particle's depth position. Figure 1 illustrates the IDPT technique, based on these assumptions and insights.

In the following sections, we describe an experimental measurement, including *in-situ* calibration and evaluation procedures, along with the IDPT image analysis and 3D localization algorithm. A list of symbols used in this work is provided in table S2, following the notation established in [33].

2.1. Experimental measurement

Before performing an experimental measurement, discrete objects (e.g. particles) are applied to the measurement surface to be 3D localized. The sample is then fixed onto the stage of an optical microscope and the surface is brought into view. To improve image contrast between the particles and the surface, we used fluorescent microparticles and epifluorescence microscopy. We define an axial depth coordinate z parallel to the optical axis, wherein $+z$ is directed towards the objective lens and z_f defines the axial position of the focal plane ($z_f = z = 0$). The lateral field is defined by in-plane coordinates, x and y , which are perpendicular to the optical axis. Images I are recorded by a single camera. The optical magnification and camera specifications (sensor format and pixel size) enable conversion

from image space (X, Y) to physical space I and determine the lateral extents of the image, or field of view.

Calibration. The distance between the microscope optics and measurement surface is scanned through an axial range h while reference images I_c are recorded at discrete axial increments Δ_{cz} (figure 1(a)). The set of N_{cal} number of reference images defines the calibration image collection, $I_c(z)$, where $(N_{\text{cal}} - 1) \cdot \Delta_{cz} = h$. The lower and upper bounds of the axial range (z^-, z^+) define the region wherein particles can be measured, $z^- < z < z^+$. Calibration is performed on the measurement surface *in-situ* to empirically map defocusing patterns to depth positions, including all sources of image variations. The axial step size Δ_{cz} should be chosen to sufficiently sample particle image defocusing as a function of depth position. Axial measurement resolution can generally be improved by using smaller step sizes but is ultimately limited by the signal-to-noise ratio of the particle images and the rate of change, or uniqueness, of the defocusing patterns with depth. The latter is determined by the microscope optics and camera pixel size while the former can, for example, be improved by averaging over multiple images acquired at each position. For particle images to uniquely encode depth positions both above and below the focal plane, the optical system must produce defocusing patterns that are measurably asymmetric about z_f . In this work, we exploit the intrinsic optical effects of our epi-fluorescence microscope as a source of latent depth-dependent information.

Evaluation. Following calibration, the lateral field of view is fixed in place and the measurement surface is repositioned within the axial range (z^-, z^+) . To measure surface shape and motion, the camera captures evaluation images I_t over time t that encode local topography data into the images of individual particles (figure 1(b)). The set of N_{test} number of evaluation images defines the test image collection, $I_t(t)$. We note that we use the variable t only to differentiate between individual images in the test image collection. The order of images and values of t can be arbitrary.

2.2. IDPT image analysis and 3D particle tracking

The IDPT algorithm analyzes the calibration and evaluation images to find matching particles in both sets of images and determine their positions by comparing the evaluation particle images against their matching calibration particle images. The core sub-routines in the IDPT algorithm (figures 1(c)–(f)) are particle identification, sub-image extraction, calibration mapping, and cross-correlation-based localization.

Particle identification. To begin to analyze individual particle images, we must first identify the particles in an image. Particles in the calibration and evaluation images are identified by applying an image segmentation algorithm to a single, specified image from each the calibration and test image collections. These images are referred to as the calibration baseline image $I_c(z^o)$ and test baseline image $I_t(t^o)$ (figure 1(c)). We

assign the baseline image for each collection to the image of best focus, in which particles can be more easily distinguished from each other and from the background. Various image segmentation methods, including adaptive thresholding [41–43], watershed segmentation [44], and machine learning algorithms [45–48], can be employed to enhance particle recognition, especially in more challenging imaging environments. In our work, we adopt a straightforward segmentation approach based on intensity thresholding combined with pixel area filtering. This method is well-suited to our experimental use-case, where the high contrast of fluorescent particle images enables reliable identification with minimal computational complexity. For each baseline image, we apply an intensity threshold to binarize the image and reveal candidate particle image contours. The threshold level is chosen to maximize the number of true particle image contours that are identified. Ideally, this can be achieved using any intensity level between the highest background pixel and the highest signal pixel of the least bright particle image. The contours are then evaluated against a pixel area filter to remove false positives, which can result from spurious noise or bright background objects. We typically identify a suitable threshold level by manual inspection and then use the pixel area filter for fine tuning. Following image segmentation and contour analysis, we assume that all valid contours are individual particle images. The baseline position (X^o, Y^o) for each particle is assigned to the discrete pixel position nearest the contour's weighted centroid. We denote individual particles using arbitrary labels k for calibration particles in the calibration images and i for target particles in the evaluation images.

Sub-image extraction. To analyze a set of target particle images in t by comparison against a series of calibration particle images in z , the local image around each particle is extracted from all images to form particle image stacks. We refer to these excised local images as sub-images, I_c^k and I_t^i . Each sub-image is defined by a square bounding box centered at the baseline position (X^o, Y^o) , to encompass the particle's image across all frames, including defocusing and in-plane motion. In this work, we discard particles whose bounding box overlaps the image borders and assign target particles an identification number $i = 1, 2, \dots, N_p''$ where N_p'' is the number of identified particles. The sizes of the calibration and target particle sub-images, L_c and L_t , are specified by the user for simplicity and can be easily determined by manual inspection. We typically define L_t first, by identifying the maximally defocused target particle image, measuring its diameter, and estimating any observed in-plane displacement. Second, we define L_c to be 2–4 pixels larger than L_t . Because the sub-images depict a fixed area in the field of view, the difference between L_c and L_t defines a local neighborhood around (X_i^o, Y_i^o) wherein the target particle's position can be reliably determined. This approach eliminates the need for image segmentation and tracking of single particles in multiple frames. The particles' sub-images are then extracted from each frame to form stacks, $I_c^k(z)$ and $I_t^i(t)$, of shape $(L_c \times L_c \times N_{\text{cal}})$ and $(L_t \times L_t \times N_{\text{test}})$, respectively (figure 1(d)). Each target particle

stack $I_t^i(t)$ encodes yet-to-be-determined 3D positions. Each calibration stack $I_c^k(z)$ maps defocusing patterns to known 3D positions. In this manner, a calibration stack is a discrete sampling of particle image defocusing for a local neighborhood in the field of view. The collection of all calibration stacks, which we refer to generally as the calibration model, is then a discrete sampling of particle image defocusing across the full field of view.

Calibration mapping. To most accurately decode a target particle's position from its sub-image, we must compare the image against the most appropriate stack of calibration particle sub-images. Subject to some criteria, a mapping algorithm f assigns each target particle to a calibration particle (figure 1(e)). To compensate for field-dependent optical effects, target particles should be mapped to calibration particles at similar (X, Y) positions. To compensate for particle-to-particle variability (e.g. non-uniform physical characteristics), target particles should be mapped to their homologous calibration particles, which is equivalent to solving the correspondence problem in computer vision [49]. These objectives can be simultaneously maximized by maintaining a fixed field of view during acquisition of the calibration and evaluation images, as described in section 2.1. Here, we match homologous particles by mapping the positions from the test baseline image (X_i^o, Y_i^o) to the calibration baseline image (X_k^o, Y_k^o) using a modified nearest neighbors approach that can compensate for slight lateral shifts in the field of view.

Cross-correlation-based localization. To determine a target particle's 3D position, its sub-image is first compared against each sub-image in the assigned calibration stack. Conceptually, the most similar calibration image corresponds to the target particle's most probable position when the image was captured (subject to the discretization of the calibration stack). A similarity function S quantifies the similarity c between the target particle image and each image in the calibration stack, $S(I_t^i, I_c^k(z))$, resulting in a stack of 2D similarity maps, $c(u, v, z)$ (figure 1(f)). Each entry in $c(u, v, z)$ represents the similarity for a particular 3D shift of I_t^i relative to $I_c^k(z)$, where the in-plane coordinates in correlation space (u, v) correspond to in-plane shifts in image space, relative to (X_i^o, Y_i^o) . For the similarity function S , we use the *match_template* function from scikit-image [50], an implementation of the normalized cross-correlation function [51]. The similarity values range from -1.0 to 1.0 , with a value of 1.0 corresponding to a perfect positive correlation and a value of 0.0 corresponding to no correlation. The position of the maximum similarity value, $c_m = c(u^*, v^*, z^*)$, corresponds to the particle's most probable discrete position. For the remainder of this work, we refer to the maximum similarity value c_m simply as the similarity. Second, $c(u, v, z)$ is interpolated around $c(u^*, v^*, z^*)$ to refine the position with sub-resolution accuracy. A 2D Gaussian function is fit to $c(u, v, z^*)$ to determine in-plane position (x_i^*, y_i^*) with sub-pixel resolution (see Methods). A parabolic three-point estimator is used to determine axial position z_i' with sub-calibration-sampling (sub- $\Delta_c z$) resolution.

See figure S4 for an illustration of the cross-correlation and interpolation procedure.

3. Generalized DPT (GDPT) algorithm

To make comparisons against our IDPT algorithm, we also implemented a conventional DPT algorithm that uses a generalized calibration model, consisting of a single calibration stack constructed from images of a single particle (referred to herein as GDPT). The generalized calibration model is indiscriminately applied to all target particles to determine their depth positions using the same sub-routine (image cross-correlation and sub- $\Delta_c z$ interpolation) as IDPT.

Our GDPT algorithm follows a typical DPT workflow [52], wherein all evaluation images are individually analyzed to first identify particles and second determine their 3D positions. To reliably identify single particle images—which can vary dramatically in size, shape, and intensity both across the field of view and between frames in typical DPT applications—it is common to pre-process the images to reduce noise and improve the effectiveness of the image segmentation algorithm [53]. In our GDPT algorithm, the images are first pre-processed by applying a 3 pixel square median filter to smooth random image noise without blurring particle image features [33]. The smoothed images are binarized using an intensity threshold and candidate particle image contours are evaluated against pixel area and eccentricity filters to remove false positives. Valid contours are assumed to be individual particle images and are fit by a square bounding box to define the particles' sub-images. The sub-images are interpolated using a 2D Gaussian function to determine the particles' in-plane positions (x_i^*, y_i^*) with sub-pixel resolution. To generate the calibration model, a single particle is selected from the calibration images and its sub-images are extracted to form a single calibration stack. All target particle sub-images are compared against the generalized calibration model, using the same sub-routine as IDPT, to determine depth position z_i' . All cross-correlations are performed on raw pixel values.

4. Results and discussion

To demonstrate our measurement technique, we first performed particle tracking on a random distribution of micro-particles immobilized on a planar substrate using IDPT and GDPT. The fixed constellation of particles enables rigorous analysis of single-particle measurement uncertainty, and the planarity of the measurement surface enables evaluation of field-dependent effects. Furthermore, since IDPT and GDPT use the same axial localization sub-routine, any differences in depth measurement accuracy can be attributed to the approach of each algorithm—namely, IDPT's individualized calibration and localization approach versus GDPT's generalized approach.

To perform the experiment, we imaged $2\text{ }\mu\text{m}$ diameter fluorescent particles on a polymer-coated glass slide (figure 2(a)) at $5\text{ }\mu\text{m}$ intervals over a $100\text{ }\mu\text{m}$ axial range (see

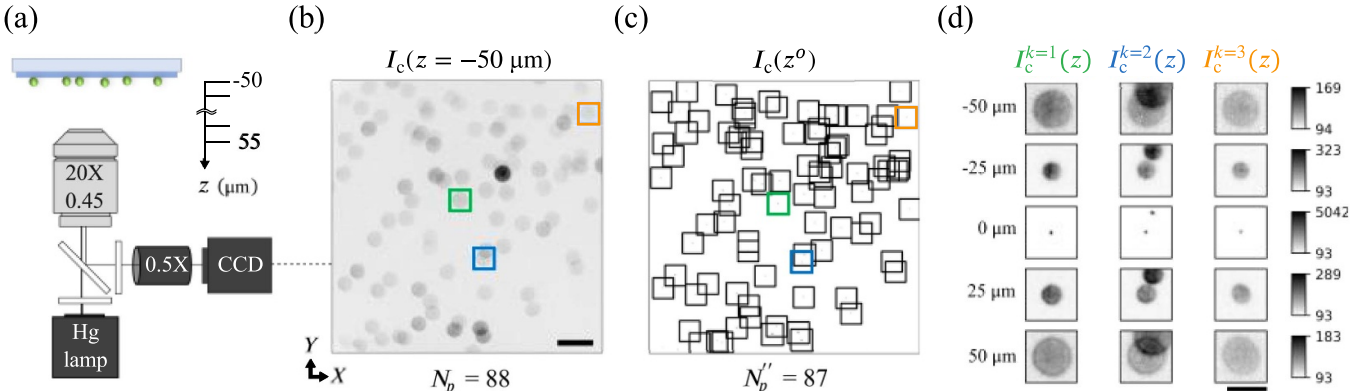


Figure 2. (a) Experimental setup. Calibration images are recorded from $z = -50$ to $55 \mu\text{m}$ using a $20\times$, 0.45NA objective with a $0.5\times$ demagnifying lens to enlarge the field of view. (b) Calibration image $I_c(z = -50 \mu\text{m})$ (contrast enhanced) showing defocused particle images. The sub-images of three representative particles are outlined for reference (green, blue, and orange boxes). Scale bar is $100 \mu\text{m}$. (c) Calibration baseline image $I_c(z^0)$, where $z^0 = z = 0 \mu\text{m}$, with particle sub-images outlined in black. (d) Sub-images from three representative calibration stacks $I_c^k(z)$, $k = 1$ (green), 2 (blue), and 3 (orange) (indicated in (b) and (c) by color), at depth positions $z = -50$, -25 , 0 , 25 , and $50 \mu\text{m}$. Particle image intensities are collectively rescaled from 0 to 1 at each depth for visual contrast. Colorbars show the raw maximum and minimum pixel values of the three sub-images at each depth. Scale bar is $50 \mu\text{m}$.

Methods for more details) and evaluated the measurement performance of IDPT and GDPT using several metrics, defined in the following sections. Calibration images were recorded in $1 \mu\text{m}$ increments from $z = -50$ to $55 \mu\text{m}$ (figure 2(b)). Particles that overlapped the image borders in any frame were excluded from our analysis. With respect to this criterion, we manually inspected the images and identified $N_p = 88$ number of measurable particles per image. Using IDPT, we identified $N_p' = 87$ particles (figure 2(c)) using calibration and target particle sub-image sizes of 43 pixels and 37 pixels, respectively, which were sufficient to accommodate the particles' defocused images all frames (figure 2(d)). For GDPT, the number of identified particles per image varied from a maximum of 75 to a minimum of 16, due to the occurrence of overlapping particle images and the limitations of our GDPT image segmentation algorithm. We selected an isolated particle from the center of the field of view to generate GDPT's generalized calibration model—corresponding to the same particle as $I_c^{k=1}(z)$ in figure 2(d).

For this comparative assessment, we define the number of measured particles per image N_p' as the number of identified particles per image N_p'' minus the number of measurements discarded as outliers [54]. We considered outliers to be measured depth positions occurring in the opposite half of the focal plane (i.e. opposite z_f) relative the known depth position. We refer to these depth measurement errors specifically as focal plane bias errors. For depth positions near z_f , we only discarded focal plane bias errors of more than $5 \mu\text{m}$ (see table S5). For GDPT, it was necessary to cull additional measurements with large, non-representative errors resulting from overlapping or partially segmented particle images, which is a common problem in DPT [33, 53, 55]. We found we could remove these outliers by discarding measurements with a similarity c_m less than 0.5, axial error greater than $5 \mu\text{m}$, or in-plane error

greater than 2 pixels. See table S6 and figure S7 for a comprehensive outlier analysis. Following, we evaluated the measurement performance of IDPT and GDPT at each depth position in terms of similarity, relative number of measured particles, and measurement uncertainty.

First, we compare the measured similarities between the target particle images and each calibration model, since higher similarities should correspond to more accurate positions. Figure 3(a) shows the local mean similarity of the measured particles evaluated at each depth, $\bar{c}_m(z)$. Naturally, a particle's distance from the focal plane affects the size, shape, and intensity of its recorded image, and these morphological changes affect the cross-correlation similarity between particle images. Specifically, $\bar{c}_m(z)$ is lower both near focus, where light from the particles is discretized across relatively few pixels, and towards the edges of the axial range, where signal-to-noise ratio is lower because the particle images are more spread out. Across all axial positions, IDPT's local mean similarity is greater than GDPT's; the individualized calibrations improve correlation between the model and target particle images. The difference in $\bar{c}_m(z)$ between IDPT and GDPT is fairly constant across the axial range—deriving from both random and systematic variations between target particle images (note S8) that, in effect, represent noise in comparison against GDPT's generalized calibration model. Over the entire axial range, the depth-averaged mean similarity \bar{c}_m was 0.96 for IDPT and 0.91 for GDPT.

Next, we evaluate the localization efficiency of IDPT and GDPT by comparing the number of measured particles per image (N_p') to the number of measurable particles per image (N_p). In figure 3(b), we plot the local mean relative number of measured particles $\bar{N}'_p(z)/N_p$ at each depth. Overall, IDPT measured a higher proportion of particles, with a global mean \bar{N}'_p/N_p of 0.92, compared to just 0.36 for GDPT. The

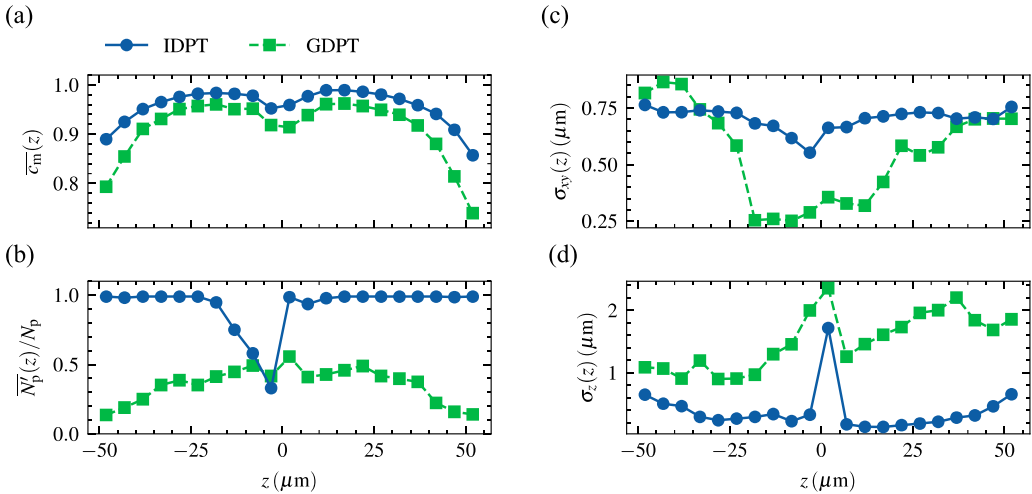


Figure 3. Comparison of depth-dependent measurement performance of IDPT (blue) and GDPT (green), showing (a) local mean similarity $\bar{c}_m(z)$, (b) local relative number of measured particles $\bar{N}'_p(z)/N_p$, (c) local in-plane measurement uncertainty $\sigma_{xy}(z)$, and (d) local depth measurement uncertainty $\sigma_z(z)$, at each depth position z .

difference in \bar{N}'_p/N_p is primarily due to the number of overlapping particle images (see figure 2(b)). A second contributing factor was focal plane ambiguity [30, 31, 37]. For our optical system, the images of particles near focus contained little to no unique information to discern the particles' direction of displacement ($+z$ or $-z$) relative to the focal plane. This issue can only be addressed by modifying the optical system, for example, using a camera with smaller pixels, using a higher magnification objective lens, or by introducing extrinsic aberrations [21, 56, 57], which is not the focus of this work. For this comparative assessment, our experimental particle images revealed measurable differences between the axial sensitivity of IDPT and GDPT at each depth position. We found GDPT was far more prone to focal plane bias errors, which accounted for a 25% decrease in \bar{N}'_p/N_p . Across the axial range, the rate of focal plane bias errors was inversely proportional to the distance from z_f , indicating that GDPT's axial sensitivity improves with particle image defocusing (figure S7). For IDPT, focal plane bias errors were negligible across most of the axial range, occurring primarily between $z = -15 \mu\text{m}$ and $0 \mu\text{m}$ (figure 3(b)). Due to the near symmetry of defocusing in our experimental images, we would expect the occurrence of focal plane bias errors to likewise be symmetric about z_f . However, this was not true for IDPT. We attribute this to a systematic pixelation effect, introduced by a slight shift in the field of view, that asymmetrically affected cross-correlative similarity near focus (note S9) [33]. We confirmed these effects by simulation using synthetic particle images with varying sub-pixel positions (note S10). We note, this in-plane shift had a negligible impact on GDPT since the collection of target particle images comprise a random distribution of natural variations and sub-pixel positions relative to the single calibration particle.

We now compare the in-plane measurement resolution of each approach, a metric of practical importance for 3D-localization-based profilometry, describing the lateral frequency of surface features that can be resolved. First, we evaluate the mean in-plane distance between measured particles using \bar{N}'_p (given in the previous section)—yielding $91 \mu\text{m}$ for IDPT and $138 \mu\text{m}$ for GDPT. The lowest achievable mean in-plane distance between particles (using $N_p = 88$) was $87 \mu\text{m}$. Next, we quantify measurement uncertainty, which is given by the root mean square error (RMSE) (see Methods). In figure 3(c), we plot the local in-plane measurement uncertainty $\sigma_{xy}(z)$ for each depth. Understandably [58–60], we found GDPT's in-plane localization sub-routine—namely, direct interpolation of the intensity image I_t^i —was generally more accurate than IDPT's indirect approach of interpolating the similarity map $c(u, v, z^*)$. However, the accuracy of GDPT's approach is subject to optical distortions, which can cause a particle's apparent in-plane position (determined by interpolation) to diverge from its true position. Correspondingly, figure 3(c) shows that GDPT's in-plane measurement uncertainty increases considerably as the particle images become increasingly defocused and diverge from the interpolating particle image model (figures S11(A) and (B)). In contrast, IDPT's in-plane uncertainty is far more consistent across the axial range, showing little dependence on depth position or, by extension, particle image overlap. Furthermore, the in-plane localization uncertainty of IDPT could likely be reduced by appropriate weighting of the similarity values prior to interpolation [61, 62]. Overall, the depth-averaged in-plane uncertainty $\bar{\sigma}_{xy}$ was $0.5 \mu\text{m}$ for GDPT and $0.7 \mu\text{m}$ for IDPT.

Building upon the previous analysis of in-plane uncertainty, we now consider the local depth measurement uncertainty $\sigma_z(z)$ (figure 3(d)). For both methods, $\sigma_z(z)$ is largest

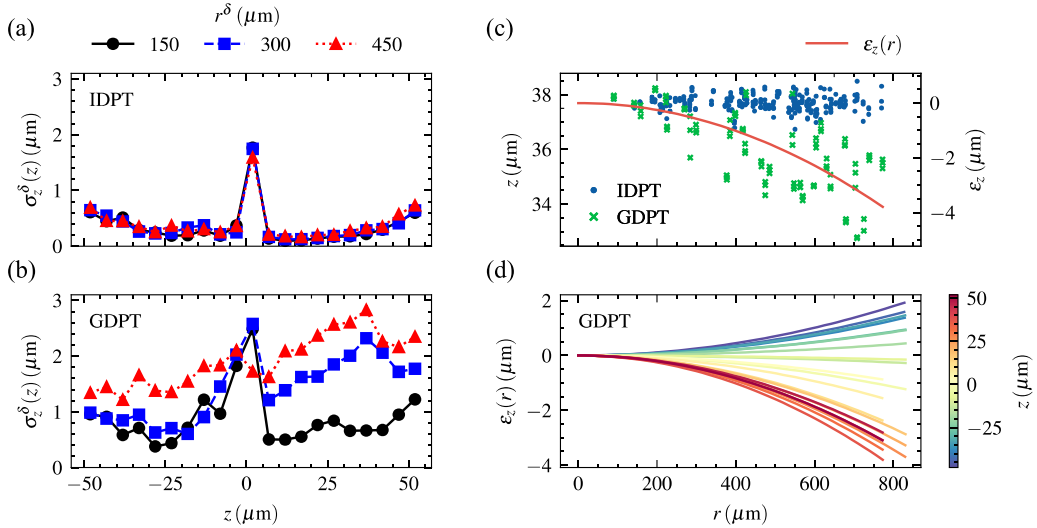


Figure 4. Depth measurement uncertainty $\sigma_z^\delta(z)$ evaluated over radial bins r^δ at each depth position z for (a) IDPT and (b) GDPT. The radial bins $r^\delta = 150\text{ }\mu\text{m}$ (black), $300\text{ }\mu\text{m}$ (blue), and $450\text{ }\mu\text{m}$ (red) correspond to radial intervals $0\text{--}225$, $225\text{--}375$, and $375\text{--}580\text{ }\mu\text{m}$, respectively. (c) Measured depth positions z'_i (z -axis) and depth errors $\varepsilon_{z,i}$ (ε_z -axis) shown as a function of r for IDPT (blue circles) and GDPT (green crosses) at $z = 37.7\text{ }\mu\text{m}$. GDPT's radially dependent z -errors ($r'_i, \varepsilon_{z,i}$) are visualized by fitting a parabolic function, $\varepsilon_z(r) = A \cdot r^2$ (red line), where A is sought by least-squares fitting. (d) Parabolic functions $\varepsilon_z(r)$ fitted to $(r'_i, \varepsilon_{z,i})$ of GDPT at each depth position (see colorbar).

near z_f , where the particles' direction of displacement relative to the focal plane could not be unambiguously resolved. Moving away from focus, the axial uncertainty of IDPT increases slowly and symmetrically as the signal-to-noise ratio decreases; though, $\sigma_z(z)$ is slightly larger for $z < 0$ due to a slight blurring of the particle images from spherical aberrations. For GDPT, $\sigma_z(z)$ is highly asymmetric about z_f . As noted earlier, random and systematic factors, like particle-to-particle variability and field-dependent optical effects, introduce variations between particle images that degrade the accuracy of generalized approaches, like GDPT. Overall, the depth-averaged axial uncertainty $\overline{\sigma}_z$ was $0.4\text{ }\mu\text{m}$ for IDPT and $1.5\text{ }\mu\text{m}$ for GDPT. Additionally, we note that the measurement performance of IDPT is generally robust to slight variations in the sizes of the calibration and target particle sub-images, L_c and L_t , respectively. For example, we varied the sizes of the calibration and target particle sub-images by ± 6 pixels and found a difference in $\overline{\sigma}_z$ of only $0.04\text{ }\mu\text{m}$ (table S12).

To estimate the influence of particle-to-particle variability, we reevaluated $\overline{\sigma}_z$ using increasingly restrictive similarity thresholds to remove lower similarity measurements (ostensibly, filtering out particles with more non-uniform physical characteristics that might contribute to increased uncertainty) (figure S13). For GDPT, we found $\overline{\sigma}_z$ could be reduced to as low as $0.7\text{ }\mu\text{m}$, although at the cost of measuring just three particles per image on average, or $\overline{N'_p}/N_p = 0.04$. Applying this same analysis to IDPT, $\overline{\sigma}_z$ could be reduced to a minimum of $0.3\text{ }\mu\text{m}$ at the marginal cost of lowering $\overline{N'_p}/N_p$ to 0.77 .

Next, we evaluate the relative importance of field-dependent effects on depth measurement accuracy. Because the severity of optical effects is often proportional to in-plane distance from the optical axis [22, 63], we evaluated the local axial uncertainty of particles divided into discrete, concentric

circular regions. We define a radial coordinate r that describes the in-plane distance from the optical axis, where $r = 0$ corresponds to the image center. We partitioned particles into radial bins r^δ and computed the local axial uncertainty $\sigma_z^\delta(z)$ for each radial bin at each depth. Whereas IDPT showed no variation in $\sigma_z^\delta(z)$ with r^δ (figure 4(a)), GDPT showed variations with r^δ and z (figure 4(b)). To visualize GDPT's r - z dependence, we fit parabolic functions to the measured particles' radial positions r'_i and axial errors $\varepsilon_{z,i}$ at each depth (figures 4(c) and (d)). We found that the curvature of the parabolic functions, albeit unpredictable, varied continuously and smoothly with z (figure S14). Following, we used the parabolic functions to remove the apparent radial-dependence embedded in GDPT's position data. This bias-error-correction method reduced $\overline{\sigma}_z$ to $1.1\text{ }\mu\text{m}$, or $0.01 h$, which is typical for DPT using custom optical setups [33], although still nearly three times larger than that of IDPT.

Lastly, we performed two separate analyses to verify that GDPT's apparent radial-dependence did not result from a flaw in GDPT's algorithm, but rather from systematic optical effects. First, we compared measurement data for the single particle that was selected to generate GDPT's calibration model, corresponding to the particle $I_c^{k=1}(z)$ in figures 2(b)–(d). We found that the similarity values and axial positions measured by IDPT and GDPT were indistinguishable (figure S15). We note, this would be true regardless of which calibration particle was selected, so long as the particle's image did not overlap its neighbors. Second, we compared our results against measurement data obtained from using the open-source 3D particle tracking software *DefocusTracker* version 2.0.0 (referred to herein as GDPTlab) [64] employing Method 1 (normalized cross-correlation) [23]. We trained GDPTlab's calibration model on the same particle as GDPT (note S16). Overall, the measurement performance

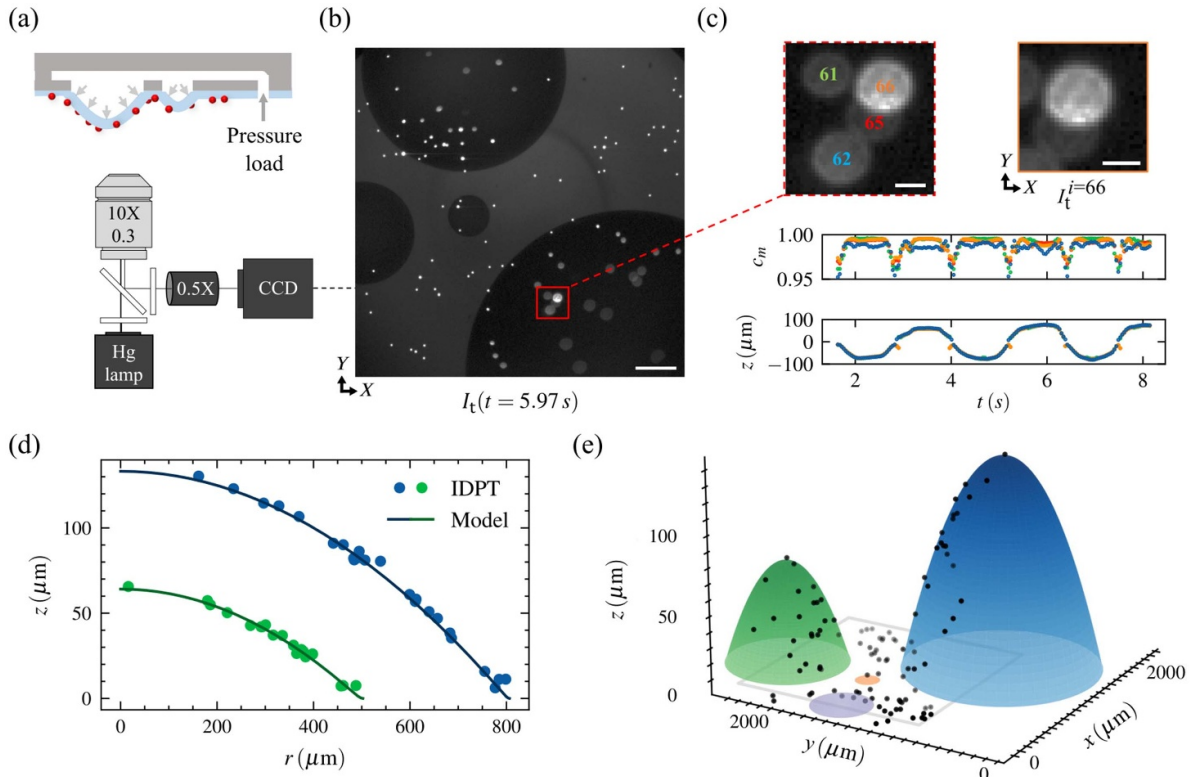


Figure 5. (a) Experimental setup. The measurement surface is imaged using a 10X, 0.3NA objective and 0.5X demagnifying lens to enlarge the field of view. (b) Evaluation image I_t ($t = 5.97$ s) showing defocused particle images due to local deformation of elastic discs of radii 800 μm (lower right), 500 μm (top left), 250 μm (left), and 100 μm (center). Image brightness is enhanced to show the background. Scale bar is 200 μm . (c) Top left: Close-up image of target particles, $i = 61, 62, 65$, and 66. Scale bar is 25 μm . Top right: Target particle sub-image $I_t^i=66$ showing in-plane displacement encoded as an off-center shift of the particle image. Scale bar is 25 μm . Bottom: Measured similarities (top) and depth positions (bottom) of target particles, $i = 61, 62, 65$, and 66 (indicated by color), during quasi-periodic pressure loading ($t \geq 1.64$ s). (d) Relative measured positions (circles) and fitted plate bending models (solid lines) for the 800 μm (blue) and 500 μm (green) radii discs in image I_t ($t = 5.97$ s). (e) Reconstructed surface topography for image I_t ($t = 5.97$ s). Measured positions are represented as black dots. The 250 μm (purple) and 100 μm (orange) radii discs are shown flat because the number of particles sampling the discs was insufficient for surface reconstruction.

of GDPTlab was comparable to GDPT and likewise demonstrated a similar radial-dependence (figures S17(A) and (B)). We obtained depth-averaged in-plane and axial uncertainties of $\bar{\sigma}_{xy} = 0.7 \mu\text{m}$ and $\bar{\sigma}_z = 2.1 \mu\text{m}$, respectively [33]. Similarly, we note that for both GDPT and GDPTlab, basing the generalized calibration model on a different particle in the field of view would reduce bias errors in that local region, but correspondingly exacerbate bias errors elsewhere [29].

To demonstrate a practical application of IDPT, we experimentally measured the simultaneous deformation of multiple elastic discs subjected to a quasi-periodic pressure load (see Methods for more details). We built a custom experimental apparatus comprising an elastic sheet bonded to a silicon substrate with etched circular holes, of radii $a = 800, 500, 250$, and 100 μm , to form suspended discs that could be inflated (figure S18). Fluorescent particles were randomly distributed onto the surface of the elastic sheet and imaged using the optical setup depicted in figure 5(a). Calibration images were acquired in 2 μm axial increments spanning a range of $h = 270 \mu\text{m}$. A series of 200 evaluation images were recorded at 24.4 fps while a handheld syringe was actuated, beginning after $t = 1.64$ s (40 images), to pressurize the discs and

displace the particles (figure 5(b)). We processed the images using IDPT to 3D localize the particles in each frame, which resulted in more than 20 000 measurements of 104 particles over an axial distance of 251 μm . See movie S1 for an animation of the measured particles' relative in-plane displacements in each frame. In figure 5(c), we focus on a cluster of four particles on the 800 μm disc, where the particles' images defocused, overlapped, and shifted in-plane relative to one another due to the spherical deformation of the underlying disc. The measured similarities and depth positions testify to the applicability of the IDPT technique and demonstrate its effectiveness for tracking dynamic surface deformations, even when particle images overlap. We believe motion blur contributed to the lower similarities and sporadic focal plane bias errors observed when the particles pass through focus. Motion blur occurs because the recorded defocused particle images represent the time-averaged intensity distribution during exposure. Here, we found particle displacements during the 40 ms exposure time exceeding 10 μm in z and 0.25 pixels in x and y .

Next, we fit plate bending models to the measured positions in each frame to evaluate the performance of IDPT and reconstruct the surface topography. We modeled the 800 μm

and 500 μm radii discs using von Karman plate theory for large deflections (see Methods). The 250 μm and 100 μm radii discs were undersampled and thus not evaluated. For each disc, we define a local radial coordinate r that describes the in-plane distance from the center of the disc. For each frame, we fit the plate model to the measured particles' relative positions (r'_i, z'_i) to determine the surface displacement profile $w(r)$ and peak deflection $w_o = w(r=0)$ (figure 5(d)). To reconstruct the surface topography, we assumed radial symmetry and extrapolated the displacement profiles beyond the field of view (figure 5(e)). See movie S2 for an animation of the reconstructed 3D surface in each frame. The mean number of measured particles relative to the number of particles on the 800 μm and 500 μm radii discs (i.e. $\bar{N_p}/N_p$ defined locally over the disc areas) was 0.87. We estimated axial measurement uncertainty by calculating the RMSE of the residuals, yielding a mean axial uncertainty $\bar{\sigma}_z$ of 3.4 μm , or 0.013 h . Despite the overall agreement between the plate models and measured positions, we observed deflection-dependent edge effects that could not be captured by our plate model. Specifically, the elastic discs bulged slightly outwards at the edges for positive deflections. These boundary compliance effects, although faithfully recorded in IDPT's measurement data, resulted in poorer local agreement with the plate model. For peak deflections $|w_o| > 15 \mu\text{m}$, we found the local mean axial uncertainty of particles near the disc edges ($r'_i/a > 0.85$) was 6.3 μm . By comparison, the local mean axial uncertainty away from the edges ($r'_i/a < 0.85$) was 1.74 μm , or 0.006 h , which is comparable to the uncertainty we found in the previous experiment ($\bar{\sigma}_z = 0.004h$). Finally, we further validated IDPT's measured positions by simulating the deformation of the 800 μm disc using COMSOL Multiphysics (note S19). This analysis found good agreement between our experimental measurements and the simulation.

5. Conclusion

In this work, we introduced IDPT, a new technique for 3D surface measurements using standard laboratory microscopes without requiring specialized optics or precise alignment. By leveraging *in-situ* calibration and each particle's unique defocusing patterns, IDPT addresses the limitations of generalized calibration models and conventional DPT methods. Our findings demonstrate that IDPT achieves greater measurement accuracy, resolution, and reliability than comparable SPT algorithms, particularly in challenging environments with field-dependent effects and optical distortions.

Through experiments involving both rigid and deformable surfaces, we demonstrated the applicability of IDPT for dynamic surface profilometry and strain visualization, underscoring its potential for use in a wider range of applications. The technique is compatible with standard microscopy setups that provide reliable defocusing patterns and sufficient image contrast, and the IDPT software package is straightforward and user-friendly, requiring minimal input from the user. These qualities distinguish IDPT from more specialized techniques.

We have made our software implementation freely available for users who wish to apply the technique, as well as researchers interested in building upon it. Our lab is currently working to expand the capabilities of the IDPT software package for more complex applications, such as flow field measurements in microfluidic systems, by implementing a fully generalizable SPT scheme on top of IDPT's local calibrations framework.

6. Materials and methods

6.1. Axial translation of particles on a planar substrate

Experimental setup and image acquisition. A 20 μm thick polymer sheet (SILPURAN 2030, Wacker) was bonded to a glass slide (CORNING, COR-2935-246) and decorated with 2 μm diameter fluorescent spheroidal micro-particles (Spherotech, FH-2056-2). The sample was placed on the stage of an inverted optical microscope (iX 73, Olympus) equipped with a 20X, 0.45NA objective lens (LUCPLFLN20X, Olympus) and a 0.5X demagnifying C-mount adaptor (C4, Olympus). The optical magnification was experimentally verified to be 10.01X using a stage micrometer with 50 μm divisions (R1L3S1P, ThorLabs). Image contrast was achieved by epifluorescence microscopy using a mercury lamp (Olympus, U-HGLGPS) for illumination. Images were captured using an electron-multiplying CCD (iXon Ultra 897, Oxford Instruments) with an exposure time of 33 ms and the electron multiplier gain turned off. The CCD consisted of a 512 \times 512 array of 16 μm pixels. The surface-bound particles were first positioned at the focal plane by adjusting the height of the objective lens until the particle images were in focus. The objective lens was then moved 50 μm away from the imaging substrate using the built-in micrometer of the microscope. Calibration images were recorded in 1 μm axial increments from $-50 \mu\text{m} \leq z \leq 55 \mu\text{m}$. At each axial position, three images were recorded and averaged together. The objective lens was repositioned at focus and then displaced 48 μm away from the imaging substrate. Evaluation images were then recorded in 5 μm axial increments across a 100 μm range using a linear stage and high-resolution micrometer with 0.5 μm sensitivity (HR-13, Newport) that was mounted to the stage of the optical microscope. Three images were acquired at each axial position for a total of 63 evaluation images.

Determination of axial position. To precisely align the depth positions of the calibration images and evaluation images relative to the focal plane, we determined the position of best focus for each particle in the field of view: First, we fit 2D Gaussian functions to the particle images to determine their intensity amplitudes in each frame. Next, we fit a one-dimensional (1D) Gaussian function to the particles' intensity amplitudes as a function of z . The peak of the 1D Gaussian function corresponds to the depth position of best focus. The 3D positions of best focus correspond to the 3D focal surface. Following, we aligned the calibration images and evaluation images to the focal plane by defining depth position z relative to the position of the focal surface at the image center. To

accurately quantify depth measurement error, it was necessary to determine the true position and orientation of the imaging substrate at each nominal depth position with greater resolution than was possible using our micrometer stage. This is because we found slight fluctuations in the orientation of the imaging substrate between depth positions and slight discrepancies between the nominal and actual depth positions. To correct for this, we fit 3D planes to the 3D positions of particles measured by IDPT at each nominal depth position. Particles with measured depth positions more than $3.25 \mu\text{m}$ from the nominal axial position were discarded prior to fitting. The positions measured by IDPT were corroborated by the positions measured by GDPT near the center of the image. Next, we took the position and orientation of the fitted planes as the true surface of the imaging substrate and removed the surface tilt from both IDPT's and GDPT's measured positions, thus analytically reorienting the imaging substrate to be perpendicular to the optical axis. The residuals quantify the accuracy of the 3D plane fits and justify the correction procedure, with an overall RMSE of $0.28 \mu\text{m}$. Using this procedure, we found the mean axial step size was $5.05 \pm 0.4 \mu\text{m}$, which is in agreement with the stated resolution of the micrometer stage.

Determination of in-plane position. To define the true in-plane position of each particle, we in-plane localized the particles using an open-source image processing software, Fiji [65], so as not to bias the calculated in-plane measurement error towards IDPT or GDPT. The calibration baseline image was binarized to identify candidate particle image contours. For each contour, the in-plane position was estimated with subpixel resolution from the intensity-weighted centroid. The measured in-plane positions were assigned nominal depth positions of $z = 0 \mu\text{m}$. To determine in-plane measurement error, we used the iterative closest point algorithm [49] to map the true in-plane positions from $z = 0 \mu\text{m}$ to the 3D positions measured by IDPT and GDPT in each frame. The residuals in x and y yield the measurement errors in x and y . We define the in-plane measurement error as the sum in quadrature of the x - and y -errors.

6.2. Dynamic surface profilometry

Test apparatus with deformable elastic discs. To fabricate the test apparatus, we first etched circular holes through a $500 \mu\text{m}$ thick silicon substrate using deep reactive ion etching. The etched pattern consisted of adjacent circles of radii $a = 800, 500, 250$, and $100 \mu\text{m}$, along with additional patterns for the inlet and outlet. A $100 \mu\text{m}$ deep channel was similarly etched into a second silicon substrate and the two wafers were bonded together using oxygen plasma bonding [66]. A $20 \mu\text{m}$ thick elastic sheet (SILPURAN 2030, Wacker) was similarly bonded over the etched circular holes to form a conduit with suspended elastic discs. To interface with the conduit, we fabricated blocks of PDMS (Sylgard 184 with 1:10 cross-linker to resin ratio) which were then hole-punched using a biopsy punch and bonded to the silicon substrate over the etched inlet and outlet holes. The PDMS block over the outlet hole was plugged so that the conduit could be pressurized. A dispensing

needle was inserted into the PDMS block over the inlet hole to create an air-tight fit. The dispensing needle was connected to a handheld plastic syringe using flexible tubing.

Experimental setup and image acquisition. Fluorescent spheroidal microparticles nominally $2 \mu\text{m}$ in diameter (Spherotech, FH-2056-2) were randomly distributed on the surface of the elastic sheet and imaged using an inverted optical microscope (iX 73, Olympus) equipped with a semi apochromatic objective (M10X, NA = 0.3, UPLFLN10X2, Olympus) and 0.5X demagnifying C-mount adaptor (C4, Olympus). Images were recorded at 24.4 fps using an electron-multiplying CCD (iXon Ultra 897, Oxford Instruments) with an exposure time of 41 ms and the electron multiplier gain set to 4. This optical setup resulted in a $1640 \times 1640 \mu\text{m}^2$ field of view, which was sufficient to simultaneously image at least one third of the area of each of the four discs. Calibration images were acquired by scanning the objective lens in $2 \mu\text{m}$ axial increments spanning an axial range of $272 \mu\text{m}$. At each axial position, 10 images were recorded and averaged together. For testing, the particle images were brought into focus. Next, a series of 200 images was acquired while a handheld syringe was actuated, beginning after 40 frames ($t = 1.64 \text{ s}$), to pressurize the sealed conduit.

Deflection analysis of deformable discs. We determined the center and radius of each disc in image coordinates by manually fitting a circle to the disc perimeter in the test baseline image. Next, we converted the position data of the circle from image coordinates to physical coordinates. The measured radii of the discs were in agreement with the nominal radii, given typical microfabrication tolerances. We identified all particles on the surface of the disc by comparing the particles' measured positions in the test baseline image against the position data of the fitted circle. For particles located within the perimeter of the disk, we transformed the particles' 3D positions (x'_i, y'_i, z'_i) to 2D positions with respect to the center of the disk (r'_i, z'_i) , where the radial coordinate r is locally defined as the distance from the disc center. To evaluate the displacement profile of each disc in each frame, we first identified and discarded measured positions that were thought to be focal plane bias errors (see **Outlier detection**, below). Second, we fit a von Karman plate model for large deflections [67] to the particle positions by least-squares fitting. The fitted plate model determines the deflection profile $w(r)$ and peak deflection w_o of the disc and the residuals determine the depth measurement error.

Outlier detection. We developed an outlier detection algorithm that compared the measured depth positions of particles on a disc to identify and discard focal plane bias errors. The outlier detection algorithm was applied separately to each frame and to the $800 \mu\text{m}$ and $500 \mu\text{m}$ radii discs. First, the mean axial position of the measured particles was determined. For large deflections, $|w_o| > 15 \mu\text{m}$, we discarded particles that were found to be opposite to the focal plane relative to the mean axial position. For small deflections, we used a modified approach that included more particles: (i) if

the standard deviation of particles' depth positions was less than $7.5 \mu\text{m}$, we discarded particles that were more than $7.5 \mu\text{m}$ from the mean axial position; (ii) if the standard deviation of the particles' depth positions was greater than $7.5 \mu\text{m}$, we did not discard any particles. This modified approach had the effect of penalizing the overall measurement uncertainty when the variance of the measured depth positions was greater.

2D Gaussian function fit to similarity maps. We fit 2D Gaussian functions to 2D similarity maps $c(u, v, z^*)$ using the Levenberg–Marquardt least-squares minimization algorithm. We used the 2D Gaussian function given by,

$$c(u, v) = A \cdot \exp \left(- \left(\frac{(u - u')^2}{2w_u^2} + \frac{(v - v')^2}{2w_v^2} \right) \right)$$

where A is the amplitude, u and v are the positions of a pixel in the u and v directions, u' and v' are the estimated positions of the peak similarity in the u and v directions, and w_u and w_v are the standard deviations in the u and v directions.

2D Gaussian function fit to intensity images. We fit 2D Gaussian functions to particle sub-images by solving the least-squares minimization problem using the Trust Region Reflective algorithm. We used the 2D Gaussian function given by,

$$I(X, Y) = A \cdot \exp \left(- \left(\frac{1}{2(1 - \rho^2)} \left[\frac{(X - X')^2}{w_x^2} - 2\rho \frac{(X - X')(Y - Y')}{w_x w_y} + \frac{(Y - Y')^2}{w_y^2} \right] \right) + B \right)$$

where A is the amplitude, X and Y are pixel positions in the x and y directions, X' and Y' are the particle's estimated positions in the x and y directions, w_x and w_y are the standard deviations in the x and y directions, ρ is a correlation coefficient between the x and y directions, and B is a constant for the background intensity.

RMSE. Measurement uncertainty σ is given by the RMSE,

$$\sigma = \sqrt{\frac{\sum_{i=1}^N \varepsilon_i^2}{N}}$$

where N is the number of measurements and ε_i is the error for each measurement.

Data availability statement

The data that support the findings of this study are openly available at the following URL/DOI: <https://doi.org/10.6084/m9.figshare.27486423.v1>.

Acknowledgments

This work was supported by Breakthrough T1D (formerly JDRF), Grant/Award Number: 2-SRA-2023-1372-M-B.

A portion of this work was performed in the UCSB Nanofabrication Facility, an open access laboratory. S.M., A.E., D.H., and S.P. conceived of the work and designed the studies. S.M. performed the experiments, wrote the algorithm, and performed the simulations. S.M., A.E., D.H., and S.P. wrote the manuscript.

Appendix

The IDPT software used in this work was implemented in Python and published under the open-source license [68]. It is available for free download at <https://github.com/sean-mackenzie/idpt>. As an example of how to use our software, the repository includes the calibration and evaluation images used for the comparative assessment presented in this work and a run-ready script to process the images using IDPT. Additionally, we provide the measurement data obtained using IDPT, GDPT, and GDPTlab, and the data analysis routines used in the preparation of this publication. Additional information is provided in the GitHub repository.

ORCID iDs

Sean MacKenzie <https://orcid.org/0000-0003-1342-5369>
 Alexander Eden <https://orcid.org/0000-0001-8765-9358>
 David E Huber <https://orcid.org/0000-0001-5707-2097>
 Sumita Pennathur <https://orcid.org/0000-0003-2227-4005>

References

- [1] Marrugo A G, Gao F and Zhang S 2020 State-of-the-art active optical techniques for three-dimensional surface metrology: a review *J. Opt. Soc. Am. A* **37** B60
- [2] Yoshizawa T (ed) 2017 *Handbook of Optical Metrology: Principles and Applications* 2nd edn (CRC Press)
- [3] Leach R (ed) 2011 *Optical Measurement of Surface Topography* (Springer)
- [4] Gåsvik K J 2002 *Optical Metrology* 3rd edn (Wiley)
- [5] Zhang W et al 2016 *Measurement Technology for Micro-Nanometer Devices* 1st edn (Wiley)
- [6] Zhou Y, Handley M, Carles G and Harvey A R 2019 Advances in 3D single particle localization microscopy *APL Photonics* **4** 060901
- [7] Von Diezmann L, Shechtman Y and Moerner W E 2017 Three-dimensional localization of single molecules for super-resolution imaging and single-particle tracking *Chem. Rev.* **117** 7244–75
- [8] Deschout H, Zanacchi F C, Mlodzianoski M, Diaspro A, Bewersdorf J, Hess S T and Braeckmans K 2014 Precisely and accurately localizing single emitters in fluorescence microscopy *Nat. Methods* **11** 253–66
- [9] Copeland C R, Dixson R G, Madison A C, Pintar A L, Illic B R and Stavis S M 2022 Localization microscopy for process control in nanoelectronic manufacturing *The 2022 Int. Conf. on Frontiers of Characterization and Metrology for Nanoelectronics (FCMN) (Monterey, CA, USA)*
- [10] Lee J R et al 2025 Roadmap on industrial imaging techniques *Meas. Sci. Technol.* **36** 013001
- [11] Yoshida S et al 2011 Development of a strain visualization system for microstructures using single fluorescent

- molecule tracking on a three-dimensional orientation microscope *Proc. SPIE* **8134** 81340E
- [12] Hazlett L, Landauer A K, Patel M, Witt H A, Yang J, Reichner J S and Franck C 2020 Epifluorescence-based three-dimensional traction force microscopy *Sci. Rep.* **10** 16599
- [13] Gordon-Soffer R, Weiss L E, Eshel R, Ferdman B, Nehme E, Bercovici M and Shechtman Y 2020 Microscopic scan-free surface profiling over extended axial ranges by point-spread-function engineering *Sci. Adv.* **6** eabc0332
- [14] McGraw C D, Stavis S M, Giltinan J, Eastman E, Firebaugh S, Piepmeyer J, Geist J and Gaitan M 2013 MEMS kinematics by super-resolution fluorescence microscopy *J. Microelectromech. Syst.* **22** 115–23
- [15] Copeland C R, McGraw C D, Geist J and Stavis S M 2018 Particle tracking of microelectromechanical system performance and reliability *J. Microelectromech. Syst.* **27** 948–50
- [16] Willert C E and Gharib M 1992 Three-dimensional particle imaging with a single camera *Exp. Fluids* **12** 353–8
- [17] Wu M, Roberts J W and Buckley M 2005 Three-dimensional fluorescent particle tracking at micron-scale using a single camera *Exp. Fluids* **38** 461–5
- [18] Sapudom J, Waschke J, Franke K, Hlawitschka M and Pompe T 2017 Quantitative label-free single cell tracking in 3D biomimetic matrices *Sci. Rep.* **7** 14135
- [19] Li Y, Mund M, Hoess P, Deschamps J, Matti U, Nijmeijer B, Sabinina V J, Ellenberg J, Schoen I and Ries J 2018 Real-time 3D single-molecule localization using experimental point spread functions *Nat. Methods* **15** 367–9
- [20] Cierpka C, Segura R, Hain R and Kähler C J 2010 A simple single camera 3C3D velocity measurement technique without errors due to depth of correlation and spatial averaging for microfluidics *Meas. Sci. Technol.* **21** 045401
- [21] Rossi M, Segura R, Cierpka C and Kähler C J 2012 On the effect of particle image intensity and image preprocessing on the depth of correlation in micro-PIV *Exp. Fluids* **52** 1063–75
- [22] Coutinho G, Moita A, Ribeiro A, Moreira A and Rossi M 2023 On the characterization of bias errors in defocusing-based 3D particle tracking velocimetry for microfluidics *Exp. Fluids* **64** 106
- [23] Rossi M and Barnkob R 2020 A fast and robust algorithm for general defocusing particle tracking *Meas. Sci. Technol.* **32** 014001
- [24] Hu Z, Xu T, Wang X, Xie Z, Luo H, He Y, Guo L, Li Y, Gan R and Lu H 2018 Fluorescent digital image correlation techniques in experimental mechanics *Sci. China Technol. Sci.* **61** 21–36
- [25] Pan B 2018 Digital image correlation for surface deformation measurement: historical developments, recent advances and future goals *Meas. Sci. Technol.* **29** 082001
- [26] Brockmann P and Hussong J 2021 On the calibration of Astigmatism particle tracking velocimetry for suspensions of different volume fractions *Exp. Fluids* **62** 23
- [27] Gentile M, Courbin F and Meylan G 2013 Interpolating point spread function anisotropy *Astron. Astrophys.* **549** 1
- [28] Babcock H P and Zhuang X 2017 Analyzing single molecule localization microscopy data using cubic splines *Sci. Rep.* **7** 552
- [29] von Diezmann L, Lee M Y, Lew M D and Moerner W E 2015 Correcting field-dependent aberrations with nanoscale accuracy in three-dimensional single-molecule localization microscopy *Optica* **2** 985
- [30] Fuchs T, Hain R and Kähler C J 2016 *In situ* calibrated defocusing PTV for wall-bounded measurement volumes *Meas. Sci. Technol.* **27** 084005
- [31] Cierpka C, Rossi M, Segura R and Kähler C J 2011 On the calibration of astigmatism particle tracking velocimetry for microflows *Meas. Sci. Technol.* **22** 015401
- [32] Zheng G, Ou X, Horstmeyer R and Yang C 2013 Characterization of spatially varying aberrations for wide field-of-view microscopy *Opt. Express* **21** 15131
- [33] Barnkob R and Rossi M 2020 General defocusing particle tracking: fundamentals and uncertainty assessment *Exp. Fluids* **61** 110
- [34] Shechtman Y, Sahl S J, Backer A S and Moerner W E 2014 Optimal point spread function design for 3D imaging *Phys. Rev. Lett.* **113** 133902
- [35] Shechtman Y, Weiss L E, Backer A S, Sahl S J and Moerner W E 2015 Precise three-dimensional scan-free multiple-particle tracking over large axial ranges with tetrapod point spread functions *Nano Lett.* **15** 4194–9
- [36] Liu S, Huh H, Lee S-H and Huang F 2020 Three-dimensional single-molecule localization microscopy in whole-cell and tissue specimens *Annu. Rev. Biomed. Eng.* **22** 155–84
- [37] Tautz K M, Gude S, Tans S J and Shimizu T S 2015 High-throughput 3D tracking of bacteria on a standard phase contrast microscope *Nat. Commun.* **6** 8776
- [38] Copeland C R, McGraw C D, Illic B R, Geist J and Stavis S M 2021 Accurate localization microscopy by intrinsic aberration calibration *Nat. Commun.* **12** 3925
- [39] Copeland C R, McGraw C D, Illic B R, Geist J and Stavis S M 2020 Particle tracking of a complex microsystem in three dimensions and six degrees of freedom 2020 IEEE 33rd Int. Conf. on Micro Electro Mechanical Systems (MEMS) (IEEE)
- [40] Rossi M 2020 Synthetic image generator for defocusing and astigmatic PIV/PTV *Meas. Sci. Technol.* **31** 017003
- [41] Yanowitz S D and Bruckstein A M 1988 A new method for image segmentation [1988 Proc.] 9th Int. Conf. on Pattern Recognition (IEEE Computer Society Press)
- [42] Zhang X-P and Desai M D 2001 Segmentation of bright targets using wavelets and adaptive thresholding *IEEE Trans. Image Process.* **10** 1020–30
- [43] Roy P, Dutta S, Dey N, Dey G, Chakraborty S and Ray R 2014 Adaptive thresholding: a comparative study 2014 Int. Conf. on Control, Instrumentation, Communication and Computational Technologies (ICCICCT) (IEEE)
- [44] Barnes R, Lehman C and Mulla D 2014 Priority-flood: an optimal depression-filling and watershed-labeling algorithm for digital elevation models *Comput. Geosci.* **62** 117–27
- [45] Dreisbach M, Leister R, Probst M, Friederich P, Stroh A and Kriegseis J 2022 Particle detection by means of neural networks and synthetic training data refinement in defocusing particle tracking velocimetry *Meas. Sci. Technol.* **33** 124001
- [46] Minaee S, Boykov Y Y, Porikli F, Plaza A J, Kehtarnavaz N and Terzopoulos D 2021 Image segmentation using deep learning: a survey *IEEE Trans. Pattern Anal. Mach. Intell.* **44** 3523–42
- [47] Sachs S, Ratz M, Mäder P, König J and Cierpka C 2023 Particle detection and size recognition based on defocused particle images: a comparison of a deterministic algorithm and a deep neural network *Exp. Fluids* **64** 21
- [48] Newby J M, Schaefer A M, Lee P T, Forest M G and Lai S K 2018 Convolutional neural networks automate detection for tracking of submicron-scale particles in 2D and 3D *Proc. Natl Acad. Sci.* **115** 9026–31
- [49] Besl P J and McKay N D 1992 A method for registration of 3-D shapes *IEEE Trans. Pattern Anal. Mach. Intell.* **14** 239–56
- [50] Van Der Walt S, Schönberger J L, Nunez-Iglesias J, Boulogne F, Warner J D, Yager N, Gouillart E and Yu T

- 2014 scikit-image: image processing in Python *PeerJ* **2** e453
- [51] Lewis J P 1995 Fast normalized cross-correlation (Industrial Light & Magic) p 8 (available at: <http://scribblethink.org/Work/nvisionInterface/nip.pdf>)
- [52] Barnkob R, Kähler C J and Rossi M 2015 General defocusing particle tracking *Lab Chip* **15** 3556–60
- [53] Rose K A, Molaei M, Boyle M J, Lee D, Crocker J C and Composto R J 2020 Particle tracking of nanoparticles in soft matter *J. Appl. Phys.* **127** 191101
- [54] Barnkob R, Cierpka C, Chen M, Sachs S, Mäder P and Rossi M 2021 Defocus particle tracking: a comparison of methods based on model functions, cross-correlation, and neural networks *Meas. Sci. Technol.* **32** 094011
- [55] Luo R and Sun Y-F 2011 Pattern matching for three-dimensional tracking of sub-micron fluorescent particles *Meas. Sci. Technol.* **22** 045402
- [56] Loi J, Qu X and Suzuki A 2023 Semi-automated 3D fluorescence speckle analyzer (3D-Speckler) for microscope calibration and nanoscale measurement *J. Cell Biol.* **222** e202202078
- [57] Rossi M and Kähler C J 2014 Optimization of astigmatic particle tracking velocimeters *Exp. Fluids* **55** 1809
- [58] Sciacchitano A 2019 Uncertainty quantification in particle image velocimetry *Meas. Sci. Technol.* **30** 092001
- [59] Chenouard N et al 2014 Objective comparison of particle tracking methods *Nat. Methods* **11** 281–9
- [60] Cheezum M K, Walker W F and Guilford W H 2001 Quantitative comparison of algorithms for tracking single fluorescent particles *Biophys. J.* **81** 2378–88
- [61] Raffel M (ed) 2007 *Particle Image Velocimetry: A Practical Guide* 2nd edn (Springer)
- [62] Ronneberger O, Raffel M and Kompenhans J 1998 Advanced evaluation algorithms for standard and dual plane particle image velocimetry *9th Int. Symp. on Applications of Laser Techniques*
- [63] Copeland C R, Ilic B R and Stavis S M 2019 Experimental variation of magnification calibration for localization microscopy *Frontiers in Optics + Laser Science APS/DLS (OSA)*
- [64] Barnkob R and Rossi M 2021 DefocusTracker: a modular toolbox for defocusing-based, single-camera, 3D particle tracking *J. Open Res. Softw.* **9** 22
- [65] Schindelin J et al 2012 Fiji: an open-source platform for biological-image analysis *Nat. Methods* **9** 676–82
- [66] Boden S, Karam P, Schmidt A and Pennathur S 2017 A process to fabricate fused silica nanofluidic devices with embedded electrodes using an optimized room temperature bonding technique *Appl. Phys. Lett.* **110** 181605
- [67] Sheploak M and Dugundji J 1998 Large deflections of clamped circular plates under initial tension and transitions to membrane behavior *J. Appl. Mech.* **65** 107–15
- [68] MacKenzie S 2024 Individualized defocusing particle tracking (available at: <https://github.com/sean-mackenzie/idpt>)